CHEMISTRY OF MATERIALS

Article

pubs.acs.org/cm

Temperature and Eu^{2+}-Doping Induced Phase Selection in $NaAlSiO_4$ Polymorphs and the Controlled Yellow/Blue Emission

Ming Zhao,[†] Zhiguo Xia,*[,†] Maxim S. Molokeev,[‡,§,∥] Lixin Ning,*[,⊥] and Quanlin Liu[†]

[†]The Beijing Municipal Key Laboratory of New Energy Materials and Technologies, School of Materials Sciences and Engineering, University of Science and Technology Beijing, Beijing 100083, China

[‡]Laboratory of Crystal Physics, Kirensky Institute of Physics, Federal Research Center KSC SB RAS, Krasnoyarsk 660036, Russia

[§]Siberian Federal University, Krasnoyarsk 660041, Russia

[∥]Department of Physics, Far Eastern State Transport University, Khabarovsk 680021, Russia

[⊥]Anhui Key Laboratory of Optoelectronic Materials Science and Technology, Department of Physics, Anhui Normal University, Wuhu, Anhui 241000, China

Supporting Information

ABSTRACT: The union of temperature-dependent phase transition and relating structural transformation via modification of chemical compositions is of fundamental importance for the discovery of new materials or their functional properties optimization. Herein, the synthesis temperature and Eu^{2+}-doping content induced phase selection and variations of the local structures in nepheline, low-carnegieite and high-carnegieite types of $NaAlSiO_4$ polymorphs were studied in detail. The luminescence of Eu^{2+} in low-carnegieite and nepheline phases shows blue (460 nm) and yellow (540 nm) broad-band emissions, respectively, under near-ultraviolet excitation. The photoluminescence evolution can be triggered by the different synthesis temperatures in relation to the Eu^{2+}-doping concentration, as corroborated by density functional theory calculations on the local coordination structures and corresponding mechanical stabilities in terms of the Debye temperature. The fabricated white light-emitting diode device with high color rendering index demonstrates that the multicolor phosphors from one system provides a new gateway for the photoluminescence tuning.

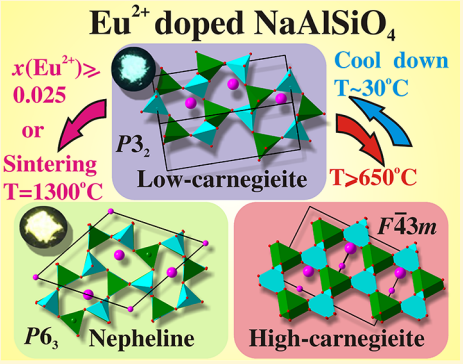

INTRODUCTION

Insight into the crystal structures and phase transitions of the solid-state compounds is important for the discovery of new materials and understanding of the attractive physical properties.[1−3] In particular, the formation of different polymorphs in one system is highly challenging for the development of novel functional materials. Moreover, the stability of polymorph depends upon the formation conditions and accordingly they exhibit interesting crystallochemical properties.[4−7] Photoluminescence of rare earth (RE) ions in inorganic hosts are sensitive to the local coordination environment, and hence, the RE phosphors can realize multicolor emission enabling different illumination and display applications represented by the white light-emitting diodes (WLEDs).[8−10] Therefore, the temperature-/pressure-dependent phase transition and structural transformation that originated from the chemical composition variation, also called the chemical-pressure effect, in one solid-state material system can bring great opportunity for the discovery of new functional properties or tuning of their physical properties, especially acting as a powerful strategy for photoluminescence tuning of inorganic phosphors.[11,12]

$NaAlSiO_4$ possesses different polymorphic forms, but has been reported only as yellow-emitting phosphors upon Eu^{2+} doping, and the exact crystal structure of low carnegieite has not yet been clearly determined until now.[13−17] In this work, the synthesis temperature and Eu^{2+}-doping induced phase selection in different nepheline (N-NASO), low-carnegieite (L-NASO), and high-carnegieite (H-NASO) types of $NaAlSiO_4$ polymorphs have been studied in detail, and the Eu^{2+}-doping content induced phase selection and controlled yellow/blue emission tuning have been further used to identify phase relations between the N-NASO and L-NASO phases. Density functional theory (DFT) calculations on local coordination structures and mechanical stabilities in terms of the Debye temperature have been performed to understand the intrinsic phase formation and photoluminescence evolution mechanism. The design principle on multicolor phosphors from different polymorphs in one system may open a new way for photoluminescence tuning.

Received: June 19, 2017
Revised: July 4, 2017
Published: July 7, 2017

DOI: 10.1021/acs.chemmater.7b02548
Chem. Mater. 2017, 29, 6552−6559

EXPERIMENTAL SECTION

Materials and Preparation. The powder samples of NaAlSiO$_4$:Eu^{2+} were prepared by the solution method using proper amounts of Al(NO$_3$)$_3$·9H$_2$O (A.R., Aladdin), NaNO$_3$ (A.R., Aladdin), Si(OC$_2$H$_5$)$_4$ (TEOS; 99.999%, Aladdin), and Eu(NO$_3$)$_3$·6H$_2$O (99.9%, Aladdin) as starting materials. The ratio of NaNO$_3$, Al(NO$_3$)$_3$·9H$_2$O, and TEOS is 1.4:1.4:1. All reagents were dissolved in water (solution A) with the exception of TEOS, which was mixed with ethanol (solution B). After solutions A and B were prepared, they were thoroughly mixed together. The mixtures were dehydrated in an oven at 120 °C until the solvent dried completely, as also was carried out in a previous paper.[18] The dried samples were ground into fine powders and then sintered at different temperatures (as pointed out below) for 3 h in a tube furnace under a reducing atmosphere of N$_2$−H$_2$ (5%). After furnace cooling to room temperature, the samples were ground again for further analysis.

Characterization. The powder X-ray diffraction (XRD) patterns were measured using a D8 Advance diffractometer (Bruker Corporation, Germany) operating at 40 kV and 40 mA with monochromatized Cu Kα radiation (λ = 1.5406 Å). The in situ variable temperature powder X-ray diffraction (VT-XRD) data were collected on X'Pert MRD diffractometer with a high-temperature reactor chamber (AntonPaar XRK 900) attached. Crystal structure solving and Rietveld refinements were performed by using TOPAS 4.2 software. ^{29}Si and ^{26}Al solid-state nuclear magnetic resonance (NMR) spectra were obtained on a solid-state Bruker 400WB AVANCE 3 at 16/20 kHz. Thermogravimetric analysis and differential thermal analysis (TG−DTA) were performed on a SIMULTANEOUS DTA-TG apparatus at 10 °C min^{-1} in an air flow from room temperature to 800 °C.

The photoluminescence (PL) and photoluminescence excitation (PLE) spectra were recorded by a fluorescence spectrophotometer (F-4600, HITACHI, Japan) equipped with a photomultiplier tube operating at 400 V and a 150 W Xe lamp as the excitation source. The internal quantum efficiency was measured by the FLS920 fluorescence spectrophotometer (Edinburgh Instruments Ltd., U.K.) with the Xe900 lamp used as an excitation source, and white BaSO$_4$ powder was used as a reference for absorption correction. For the white LEDs lamp fabrication, near-UV LED chips (λ = 395 nm) were combined with a blue-emitting L-NASO:0.01Eu^{2+}, yellow-emitting N-NASO:0.03Eu^{2+}, and red-emitting Sr[LiAl$_3$N$_4$]:0.01Eu^{2+} phosphors prepared in our lab.[19] Optical properties, including the electroluminescence (EL) spectrum, color temperature (CCT), color-rendering index (Ra), and CIE color coordinates of the LEDs, were characterized using a PMS-80 Plus UV−vis−near IR Spectrophotocolorimeter system.

COMPUTATIONAL METHODOLOGY

The atomic structures of the Eu-doped NaAlSiO$_4$ systems were fully optimized by periodic DFT by using the PBE functional[20] with a Hubbard U parameter of 2.5 eV for the Eu 4f electrons[21,22] and the PAW approach,[23] as implemented in the VASP code.[24,25] The electrons of Eu($5s^25p^64f^76s^2$), Na($2p^63s^1$), Al($3s^23p^1$), Si($3s^23p^2$), and O($2s^22p^4$) were treated as valence electrons. The "stress−strain" method[26] was employed to calculate the elastic constants, based on which the elastic moduli were derived with the Voigt−Reuss−Hill approximations.[27] The Debye temperature Θ_D was then determined with the quasiharmonic model,[28] which has been demonstrated previously to be an accurate approximation.[29] The geometry optimizations were performed until the total energies and the forces on the atoms converged to 10^{-6} eV and 0.01 eV Å^{-1}, respectively. A 2 × 2 × 2 k-point grid was used for L-NASO:0.083Eu^{2+} and N-NASO:0.143Eu^{2+}, while for L-NASO:0.333Eu^{2+}, a 4 × 4 × 2 k-point grid was adopted. The cutoff energy for the plane wave basis was set to 530 eV.

RESULTS AND DISCUSSION

NaAlSiO$_4$ can exist in different polymorphic forms, namely, N-, L-, and H-NASO phases, as was mentioned previously.[17] The XRD patterns obtained with different synthesis temperatures for the mixed starting materials with the nominal composition of NaAlSiO$_4$ are shown in Figure S1 in the Supporting Information. The N-NASO phase was obtained when the reaction temperature reached 1200 °C, whereas L-NASO phase can be formed when the reaction temperature was increased up to 1300 °C. It is found that N-NASO:Eu^{2+} shows yellow emission; however, L-NASO:Eu^{2+} exhibits blue emission when the Eu^{2+}-doping concentration is fixed at 0.01 mol. Figure S2 presents the Rietveld refinement of the XRD patterns and the crystal structure of N-NASO, which belongs to hexagonal structure ($P6_3$) with parameters close to those previously reported.[30] Therefore, the previously reported N-NASO crystal structure was taken as the starting model for Rietveld refinement. The final model shows a high thermal parameter of Na ion in Na1 site similar to earlier results,[30] and an unusual short bond length $d_{(Al_2-O_5)}$ = 1.27 Å. Since the Bragg R-factor in the previous report was not very good (R_B = 9.67%),[30] it was decided to improve the known structural model. The high thermal parameter of the Na1 ion is supposedly associated with fractional occupation of this site and then it was allowed to be refined. Bragg R-factor of our model dropped down to R_B = 1.80%, the occupancy of Na1 site by Na ions was refined to 0.49(1), and all bond lengths become acceptable: $d_{(Al-O)}$ = 1.46(4)−1.74(2) Å, $d_{(Si-O)}$ = 1.60(3)−1.82(4) Å. This means that the actual formula is Na$_{0.873(3)}$AlSiO$_{3.937}$ instead of NaAlSiO$_4$ with nepheline phase and there are vacancies in Na and O sublattices. The main parameters of refinement, coordinates of atoms, and main bond lengths are summarized in Tables S1 and S2, respectively, and the updated crystallographic information file (CIF) of N-NASO is presented in the Supporting Information.

Figure 1a schematically illustrates the structural phase transformation relations among the three NaAlSiO$_4$ polymorphs at different experimental conditions. However, the crystal structure of L-NASO was not solved previously and even the crystal system remains questionable. Comparison of the as-measured powder pattern of L-NASO with PDF-2 database showed three matches: PDF-52-1342 (synthetic L-NASO, *Pmaa* space group, quality unknown);[17] PDF-11-220 (L-NASO, unknown system, quality questionable),[31] and PDF-33-1203 (L-NASO, triclinic system, quality indexed).[32] The crystal structure of L-NASO can be solved using the parent phase (H-NASO) information and its transformation under phase transition depending on the temperature variation. Therefore, in situ temperature-dependent XRD patterns of as-prepared L-NASO were measured from room temperature to 800 °C (Figure 1b). At 650 °C (or higher), H-NASO phase was formed, and phase transition temperature appears at about 650 °C. As also demonstrated by the TG-DTA result, it is apparent that the phase transition occurs at 650 °C during the heat treatment of L-NASO in air (Figure S3), which agrees with the above result of in situ XRD experiment above. However, H-NASO phase cannot be obtained at room temperature after cooling. Figure S4 gives the Rietveld analysis pattern for the as-obtained X-ray powder diffraction data and the crystal structure of H-NASO. The refined occupancy value of Na2 site is equal to 0.14(2) and the chemical formula can be written as Na$_{1.035(5)}$AlSiO$_4$, which suggests the existence of vacancies in

DOI: 10.1021/acs.chemmater.7b02548
Chem. Mater. 2017, 29, 6552−6559

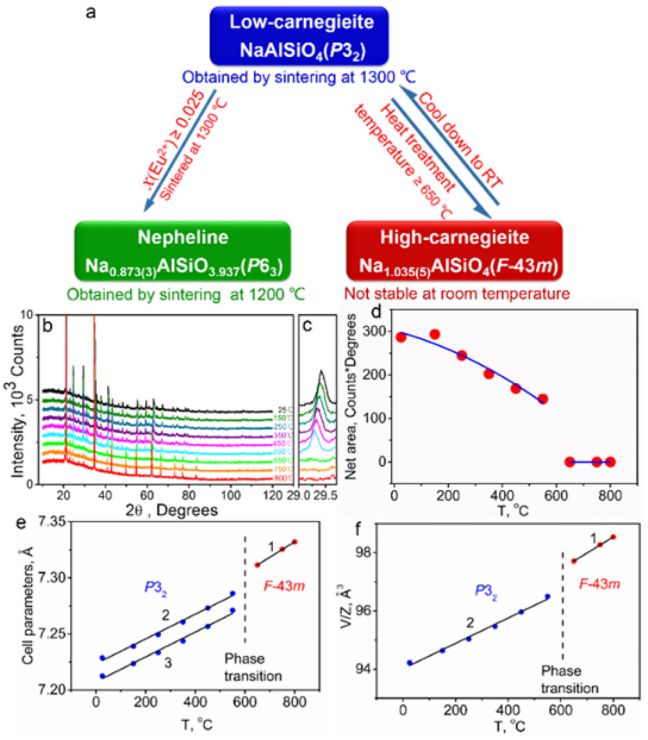

Figure 1. (a) Schematic illustration of the structural phase transformation relations among the nepheline, low-carnegieite, and high-carnegieite $NaAlSiO_4$ in different experimental conditions. (b) In situ temperature-dependent X-ray powder patterns showing the phase transition from low-carnegieite (top) to high-carnegieite (bottom) under heating. (c) Transformation of superstructure peak (near 29.5°) under heating. (d) Net area under this peak near 29.5°. (e) Temperature dependence of cell parameters: a (curve 1) of high carnegieite; $a \times 2^{1/2}$ (curve 2) and $c/3^{1/2}$ (curve 3) of low carnegieite. (f) Temperature behavior of asymmetric unit cell volume V/Z for the high carnegieite (curve 1) and low carnegieite (curve 2).

Al/Si sublattices in H-NASO. Both of the two Na sites have a coordination number (CN) of 12. The detailed results of the structural refinement and main bond lengths of H-NASO are presented in Tables S3 and S4, and the CIF of H-NASO can also be found in the Supporting Information.

As evident in Figure 1b, impurity peaks are present in temperature-dependent XRD patterns of L-NASO, and the peaks cannot be removed by heating and also cannot be indexed by well-known parent phase $F\bar{4}3m$ (H-NASO, 800 °C). It should be noted that every time small impurity peaks prevent good indexing and this could be the main reason for the failure to find the symmetry in the past. Indexing procedure using 22 first peaks of L-NASO besides impurity peaks in program TOPAS 4.2 gave primitive trigonal/hexagonal unit cell with a = 5.1082 Å, c = 12.4961 Å (GOF = 29.86). Such crystal system was found for the first time and Le-Bail profile fitting using whole pattern proved that this unit cell can index all peaks besides mentioned impurity peaks. Moreover, the system of superstructure peaks in L-NASO was found and investigated. These peaks were easily differentiated from the low-intensity impurity peaks because their intensities decrease under heating. The reason for such behavior is that order parameters values decrease with heating and even become zero at phase transition point and higher. One representative superstructure peak is shown in Figure 1c. One can see that its net area first decreases and, at phase transition, it changes with a jump down to zero (Figure 1d). Namely, this peak can be indexed with rational indexes ($^4/_3$, $^4/_3$, $^4/_3$) using parent unit cell ($F\bar{4}3m$) and of course it is prohibited in parent phase. The phase transition breaks cubic symmetry, new translations appear, and indexes of such superstructure peaks become integer and valid. It was found that all superstructure peaks can be described by the emergence of instability at the ($^1/_3$, $^1/_3$, $^1/_3$) LD point of the Brillouin zone of the parent $F\bar{4}3m$ unit cell (hereinafter the designation of irreducible representations (irrep) and points of Brillouin zone are given in accordance with reference books).[33,34]

To resolve the space group and obtain a starting structural model of L-NASO, the group theory and program ISODISTORT[35] were used. The structure of H-NASO ($F\bar{4}3m$) was uploaded to the program and Method 2 "General method—search over specific k points" was used with LD point ($^1/_3$, $^1/_3$, $^1/_3$). Hexagonal system was excluded by the program because parent cubic phase had no sixfold axis. Also, it should be noted that there are no centrosymmetric phases in the list because the parent phase ($F\bar{4}3m$) has no center of inversion. Anyway, at least three trigonal space groups were found with the smallest primitive cell volume: (1) $P3m1$ with the unit cell transformation matrix ($^1/_2$, $-^1/_2$, 0),($-^1/_2$, 0, $^1/_2$),(-1, -1, -1); (2) $P3$ (0, $-^1/_2$, $^1/_2$),($-^1/_2$, $^1/_2$, 0),(-1, -1, -1); (3) $P3_2$ (0, $-^1/_2$, $^1/_2$), ($-^1/_2$, $^1/_2$, 0), (-1, -1, -1). All these unit cells have the same cell parameters that are similar to previously indexed a = 5.1082 Å, c = 12.4961 Å. Space groups $P3m1$ and $P3$ were excluded from consideration because they generate superstructure peaks (0 0 1) and (0 0 2) which are actually absent on experimental patterns. Space group $P3_2$ has one extinction rule and all reflections (0 0 L), $L \neq 3n$, should be excluded. Namely, this extinction rule makes intensities of reflections (0 0 1), (0 0 2) become zero, and therefore, $P3_2$ was chosen as the first candidate to solve and refine the crystal structure. The LD3LE3 irrep drives this PT, and the transformation can be written as $F\bar{4}3m \leftrightarrow (\eta1, 0, \eta2, 0; 0, 0, 0, 0; 0, 0, 0, 0; 0, 0, 0, 0) \leftrightarrow P3_2$, where $\eta1$ and $\eta2$ are the components of critical order parameters. Finally, the crystal structure of the low carnegieite was solved by a distortion-mode refinement of X-ray data using the TOPAS 4.2 program, with a file generated by ISODISPLACE using the initial parent phase and LD3LE3 irrep distortion. The amplitudes of critical symmetry modes were used to find a structural model by the simulated anneal method. Then all atomic coordinates were refined independently by the Rietveld method. The isotropic thermal parameters of Na, Al, and Si atoms were refined independently, but a uniform thermal parameter was taken for all O atoms. Figure 2a presents the difference Rietveld plot of of L-NASO demonstrating the goodness of the fit and the high crystalline phase purity. The main parameters obtained from processing and refinement of L-NASO, as well as the main bond lengths, are given in Tables S5 and S6, and the CIF of L-NASO is presented in Supporting Information. Moreover, bond valence sums (BVS) calculated using bond lengths and b_0, b values for Na^+, Al^{3+}, and Si^{4+} from previously reported work[36,37] gave BVS(Na^+) = 0.96, BVS(Al^{3+}) = 3.04, BVS(Si^{4+}) = 3.91 which are very close to formal charges +1, +3, and +4, respectively. The crystal structure was further checked for possible missed symmetry elements by the PLATON program[38] and the result shows that there are no missed elements and the space group cannot be increased. Additional tests on pseudosymmetry search in the structure were performed by Bilbao Crystallographic Server.[39] It indicates that the structure can be

DOI: 10.1021/acs.chemmater.7b02548
Chem. Mater. 2017, 29, 6552−6559

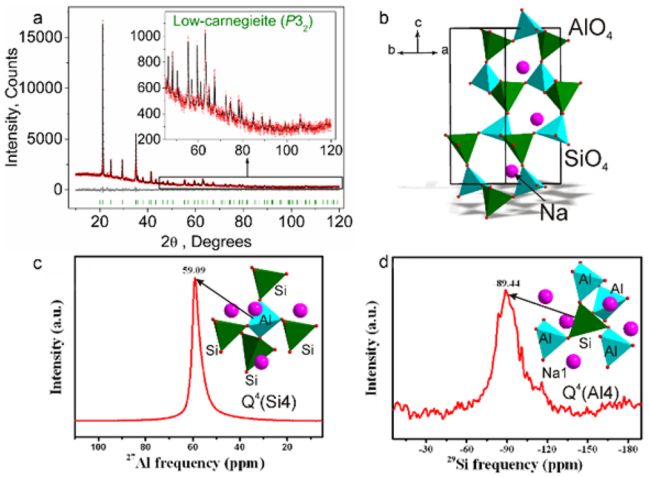

Figure 2. (a) Difference Rietveld plot of L-NASO demonstrating the goodness of the fit and high crystalline phase purity. (b) Unit cell structure of L-NASO with representative coordination polyhedra. (c) ^{27}Al NMR and (d) ^{29}Si NMR of L-NASO and the inset shows the local structure of Al and Si atoms in L-NASO.

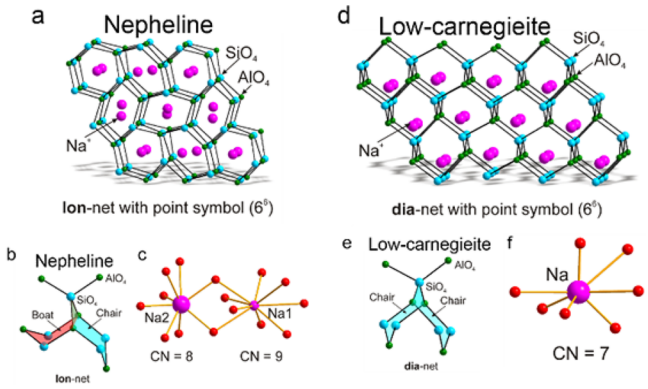

Figure 3. Topology nets of (a) nepheline and (d) low carnegieite. The AlO_4 and SiO_4 represented as spheres. Coordination SiO_4 (or AlO_4) node by other nodes is different for (b) nepheline and (e) low carnegieite, showing chair + boat and chair + chair conformations, respectively. Na coordination of (c) nephiline and (f) low carnegieite.

transformed into the $P3m1$ space group, but the resultant atom shifts are so large that the crystal structure becomes very distorted and unacceptable. Anyway, the search of crystal structures in the $P3m1$ group was also performed and the result was again negative. Thus, it was concluded that the $P3_2$ group is appropriate and correct for L-NASO.

Figure 2b shows the unit cell structures of L-NASO along with representative coordination polyhedra, in which SiO_4 and AlO_4 tetrahedra are linked to each other with sharing corner oxygen atoms, and the space around them is filled by Na^+ ions. To verify further the local structures of Al and Si atoms in L-NASO, we measured the ^{27}Al and ^{29}Si MAS NMR spectra. The ^{27}Al NMR spectrum of L-NASO (Figure 2c) shows one narrow peak at 59.09 ppm, which reveals that the coordination number of Al ions in the crystal structure is equal to 4. Absence of peak splitting proves the existence of only one Al site in the structure. Furthermore, the value of the chemical shift (δ), using the formula $\delta = -59.965(\mathrm{T-T}) + 246.39$ and the averaged bond length $(\mathrm{T-T}) = d_{(\mathrm{Al-Si})} = 3.143$ Å, was estimated to be 57.9 ppm, also in good agreement with the experimental data.[40] ^{29}Si NMR spectra of L-NASO (Figure 2d) show a broad peak at −89.44 ppm, which demonstrates that the coordination number of Si ions in the crystal structure is also 4. The value of the chemical shift δ can be estimated using the formula $\delta = -24.336\ \Sigma\mathrm{EN}_i + 279.27$, where EN_i is the sum of the group electronegativities.[40] As the coordination of Si can be written as $Q^4(4\mathrm{Al})$, that is, Si is coordinated by 4 Al with group electronegativity $\mathrm{EN}_i = 3.7339$, the calculated value for the chemical shift of Si is equal to −84.2 ppm which is close to the observed value. The local structures of Al and Si atoms in L-NASO are also demonstrated in the inset of Figure 2c,d, respectively. Therefore, the NMR data are in good agreement with those derived from the Rietveld refinements of the crystal structure.

Except for H-NASO phase, both L- and N-NASO phases are stable at room temperature. To further compare their local coordination structures, the topological analysis of the 3D nets were implemented with AlO_4 and SiO_4 represented as spheres located at the gravity centers. The 3D net of N-NASO is the well-known lonsdaleite net with symbol *lon* or 4/6/h2 (Figure 3a), and the 3D net of L-NASO is the well-known diamond net with symbol *dia* or 4/6/c1 (Figure 3d). The Na^+ ions are located inside the voids of the nets. Actually, these nets have some relations. There exists a very rare allotrope of carbon called lonsdaleite, a diamond twin that is hexagonal rather than cubic.[41] The corresponding *lon*-net has identical point and vertex symbols compared to *dia*-net, but the structural difference is that some of the six rings are in boat rather than chair conformation (Figure 3b,e). Besides differences in the 3D nets constructed from SiO_4 and AlO_4 polyhedra, there is a difference in the Na^+ sublattices. N-NASO has two independent Na sites (Na1 in 2a and Na2 in 6c) and only Na2 is fully occupied, but Na1 is occupied partly (~49%); therefore, the chemical formula is $Na_{0.873(3)}AlSiO_{3.937}$, as discussed previously. L-NASO has only one Na site (3a) which is fully occupied by Na, so the chemical formula is $NaAlSiO_4$. The analysis of Na coordination shows further difference. N-NASO has two Na sites with CN = 8 and 9, whereas L-NASO has only one Na site in an asymmetric part of the unit cell and it has the lowest coordination number CN = 7 (Figure 3c,f).

Beyond the difference in the synthesis temperature between N-NASO and L-NASO phases, it is urgent to understand the temperature-dependent phase transition and structural transformation induced by chemical composition changes. As is known, the luminescence properties of Eu^{2+} are sensitive to the local coordination environment.[42] Thus, it is very interesting to observe the structural transformation from L-NASO to N-NASO which was triggered by the Eu^{2+} doping even if the synthesis temperature is fixed at 1300 °C, as demonstrated in Figure 1a. Figure 4a gives the XRD patterns of $Na_{1-x}AlSiO_4$:xEu^{2+} sintered at 1300 °C. As is seen from Figure 4a, if Eu^{2+} content is below 0.025, L-NASO was obtained at this synthesis temperature. However, at the same temperature, the product becomes N-NASO when Eu^{2+} content is larger than 0.025. Figure S5 shows the Rietveld refinement of the XRD diffraction patterns recorded from $NaAlSiO_4$ doped by 1 and 3 mol % Eu^{2+}, respectively, which confirms the phase formation of L-NASO and N-LASO at the same temperature, but at different Eu^{2+} contents. This is a very interesting phenomenon and the structural transformation mechanism will be given below.

DOI: 10.1021/acs.chemmater.7b02548
Chem. Mater. 2017, 29, 6552−6559

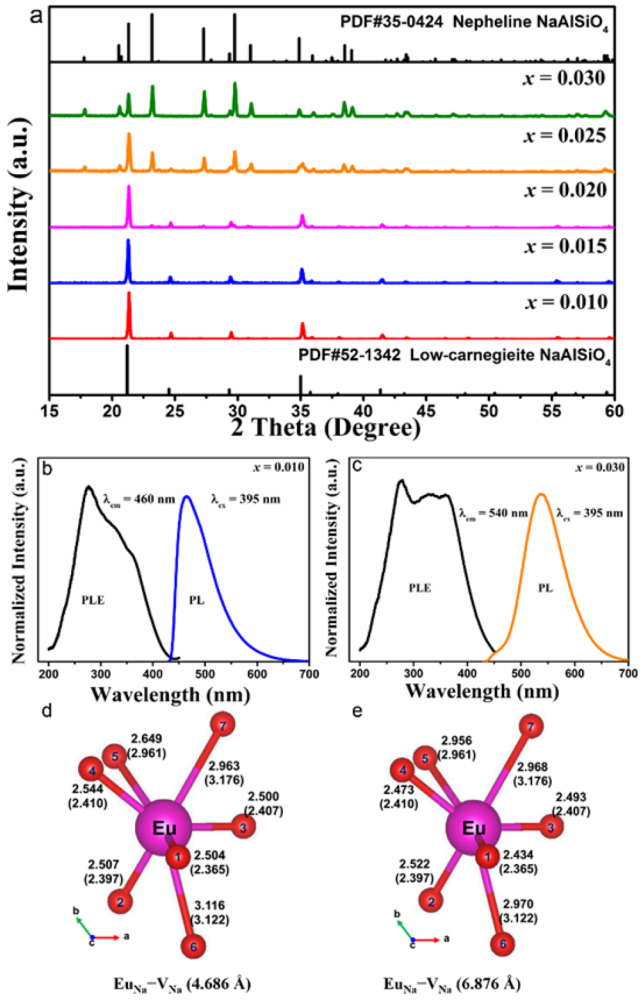

Figure 4. (a) XRD patterns of $Na_{1-x}AlSiO_4$:xEu^{2+} sintered at 1300 °C. Photoluminescence excitation and emission spectra of (b) L-NASO:0.01Eu^{2+} and (c) N-NASO:0.03Eu^{2+} sintered at 1300 °C. DFT-optimized local coordination structures of Eu^{2+} in L-NASO at the Na site with a nearby or distant V_{Na} for charge compensation. The relaxed (d) and unrelaxed (e) Eu−O distances (Å) are indicated.

Figure 4b,c show the typical photoluminescence excitation (PLE) and photoluminescence emission (PL) spectra of L-NASO:0.01Eu^{2+} and N-NASO:0.03Eu^{2+}, respectively. The samples were synthesized at 1300 °C, but they are different in the Eu^{2+} contents. In Figure 4b, the PL spectrum of L-NASO:0.01Eu^{2+} phosphor excited at 395 nm exhibits a broad asymmetric blue-emission band centered at 460 nm arising from the 5d−4f transition of Eu^{2+}. And the corresponding PLE spectrum monitored at 460 nm also shows characteristic excitation bands of Eu^{2+} ions in the range from 200 to 450 nm. The asymmetric broad emission band suggests the existence of multiple types of Eu^{2+} activators with different local environments in the phosphor. This is somewhat surprising because only one type of crystallographic Na sites exists in L-NASO (as discussed above), for which Eu^{2+} are expected to substitute on the basis of relative ionic sizes. The multiple Eu^{2+} sites could be caused by the presence of other defects required to compensate for the excessive charge of Eu_{Na} substitutions. Considering the high synthesis temperature of the material and the volatility of Na^+, we suppose that the formation of Na vacancies (V_{Na}) is most probable for the charge compensation.

To further elucidate the above point, we have performed DFT calculations on the local structures of Eu^{2+} in L-NASO. The Eu-doped L-NASO was modeled with a 2 × 2 × 1 supercell containing 84 atoms, in which one of 12 Na^+ ions was replaced by a Eu^{2+}, and another by a V_{Na} for charge compensation. The corresponding chemical formula is $Na_{1-2x}Eu_x\square_xAlSiO_4$ (x = 0.083), where the symbol □ represents the V_{Na}. Two different Eu_{Na}−V_{Na} double substitutions were considered, which are distinguished by the shortest (4.686 Å) and longest (6.876 Å) Na−Na distances in the undoped supercell, as given in Figure 4d,e. The nearest distance between Eu^{2+} ions in the supercell system is around 10.3 Å, which is large enough to neglect their mutual influence on the study of the local structure of Eu^{2+}. After geometry optimization, the calculated DFT total energies for the two supercells indicate that the nearby Eu_{Na}−V_{Na} subsititution is more stable than the distant one by ∼100 meV. This means that the two single defects prefer to be close to each other, as is expected from their opposite effective charges. Since the presence of V_{Na} at different distances would lead to slightly different local structures of Eu^{2+} (see below), we could expect the emission band of Eu^{2+} to be a asymmetrical profile (as is indeed observed experimentally in Figure 4b), with the dominant contribution from those with a nearby V_{Na} for charge compensation.

The DFT-optimized local environments of Eu^{2+} in L-NASO for the two kinds of double substitutions are shown in Figure 4d,e with the values of relaxed (d) and unrelaxed (e) bond lengths. In both cases, the incorporation of Eu^{2+} at the Na^+ site causes an anisotropic deformation of the coordination polyhedron around the dopant site (M). For the nearby (distant) Eu_{Na}−V_{Na} substitution, the distances from M to the four nearest O atoms (O1−O4) are increased by 0.093−0.139 Å (0.064−0.125 Å), whereas to the three farthest O atoms (O5−O7), the distances are decreased by 0.006−0.312 Å (0.005−0.208 Å). The average M−O distances, however, remain almost unchanged, with a decrease at the level of 0.008 Å (0.003 Å). To compare the extents of distortions in different coordination polyhedra, we employ a distortion index defined as[43]

$$D = \frac{1}{n}\sum_{i=1}^{n}\frac{|d_i - d_{av}|}{d_{av}} \quad (1)$$

where d_i is the distance from M to the ith coordinating O atom and d_{av} is the average M−O distance. We found that, upon Eu_{Na} substitution, the D value decreases from 0.126 for M = Na to 0.076 (0.088) for M = Eu with a nearby (distant) V_{Na}. Thus, the substitution reduces the irregularity of the coordination polyhedron of the dopant site. It is also interesting to observe that, with a nearby V_{Na}, the Eu^{2+} coordination polyhedron is slightly less distorted than that with a distant V_{Na}. This could lead to a smaller crystal field splitting of the Eu^{2+} 5d levels[44] and/or a smaller Stokes shift of the 4f−5d transition[45] and, hence, a larger 5d → 4f emission energy, which is consistent with the above conclusion based on the results of DFT total energies.

As is known, stability of the polymorphs depends upon the formation conditions and can be controlled by different mechanisms.[46,47] In our case, it was observed that the L-NASO phase of Eu^{2+}-doped $NaAlSiO_4$ transformed into the N-NASO with the Eu^{2+} concentration increase to a certain value (0.025), and the observed photoluminescence properties

DOI: 10.1021/acs.chemmater.7b02548
Chem. Mater. 2017, 29, 6552−6559

change accordingly. As given in Figure 4c, the emission spectrum of N-NASO:0.03Eu^{2+} contains the yellow-emission band from 430 to 700 nm consisting of a dominant peak at 540 nm and a minor shoulder peak at ~450 nm, which can be ascribed to the two different sites of Eu^{2+}. However, the yellow emission centered at 540 nm mainly contributes the as-observed PL, suggesting the preferred occupation of Eu^{2+} which will be discussed later. The excitation spectrum monitored at 540 nm exhibits a broad band ranging from 200 to 450 nm with two main peaks at 278 and 330 nm, respectively.[15] To substantiate the analysis, DFT calculations were performed for N-NASO:Eu^{2+}. The crystal was modeled on the basis of an ordered host structure containing one Na1 atom and six Na2 atoms in the unit cell, one of which was replaced by a Eu atom corresponding to the chemical formula $Na_{1-x}Eu_xAlSiO_4$ (x = 0.143) that is neutral in charge. After optimization of the atomic structure, the DFT total energies reveal that the Eu_{Na2} substitution is much more stable (by 467 meV) than the Eu_{Na1} one, which means that most of the Eu^{2+} ions are located at Na2 sites. This is consistent with the experimental observation of a dominant emission band at 540 nm, corresponding to the Eu^{2+} emission at Na2 sites.

The phase transformation depending on Eu^{2+}-doping content could be mainly attributed to the deterioration of the mechanical stability of L-NASO at high temperatures, as a result of the less rigidity of the sample when more V_{Na} are present along with Eu_{Na}. To explore this, we have calculated elastic constants and moduli of L-NASO:xEu^{2+} (x = 0, 0.083, 0.333), from which the Debye temperature (Θ_D) was determined. Θ_D has been demonstrated to be a useful proxy for structural rigidity.[29,48] Here, the L-NASO:0.333Eu^{2+} system was modeled with an L-NASO unit cell (21 atoms), where two of the three Na atoms were replaced by a Eu_{Na}–V_{Na} double substitution with a distance of 4.686 Å. The results are given in Table 1. It shows that the incorporation of Eu_{Na}–V_{Na} decreases

Table 1. Calculated Bulk Modulus (B_H), Shear Modulus (G_H), Poisson Ratio (ν), and the Debye Temperature (Θ_D) for L-NASO:xEu^{2+} (x = 0, 0.083, 0.333) and N-NASO:xEu^{2+} (x = 0.143) with the DFT-PBE Method

	d(Eu_{Na}–V_{Na})	B_H (Gpa)	G_H (Gpa)	ν	Θ_D (K)
L-NASO:xEu^{2+}					
x = 0		62.8	37.6	0.251	541
x = 0.083	d = 4.686 Å	56.4	33.7	0.251	496
x = 0.083	d = 6.876 Å	55.5	33.4	0.250	494
x = 0.333	d = 4.686 Å	51.6	32.7	0.239	447
N-NASO:xEu^{2+}					
x = 0.143		47.2	39.6	0.172	522

the structural rigidity of the L-NASO phase, changing the value of Θ_D from 541 K for x = 0 to 494–496 K for x = 0.083, and to 447 K for x = 0.333. For comparison, we have also calculated Θ_D of N-NASO:0.143Eu^{2+}, which has a Θ_D value (522 K) larger than that of L-NASO:0.083Eu^{2+}, even if it is located at a higher doping concentration level. From these results, we can conclude that, in the L-NASO phase, the doping of Eu_{Na} was accompanied by the formation of V_{Na} for charge compensation, which decreases the mechanical stability of the phase at high temperatures and drives the transformation into N-NASO phase with a smaller fraction of Na atoms than that in L-NASO. The results are excellent proof to the experimental observation of the phase transformation.

Finally, the corresponding CIE chromaticity diagram calculated from their emission spectra of L-NASO:0.01Eu^{2+} and N-NASO:0.03Eu^{2+} phosphors and their corresponding digital images upon the 365 nm UV lamp are shown in Figure 5a. Furthermore, the internal quantum efficiency of L-

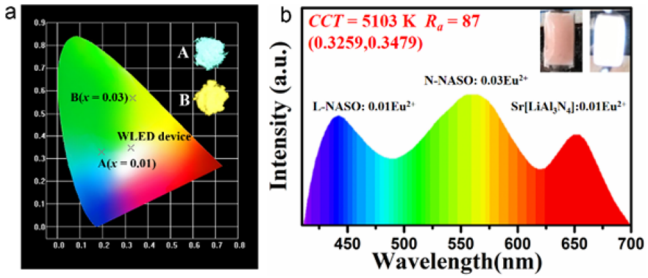

Figure 5. (a) CIE chromaticity diagram and digital photographs of $NaAlSiO_4$:xEu^{2+} (x = 0.01 and 0.03) sintered in 1300 °C and the fabricated WLED device. (b) EL spectrum of a WLED device fabricated with blue L-NASO:0.01Eu^{2+}, yellow N-NASO:0.03Eu^{2+}, and red Sr[$LiAl_3N_4$]:0.01Eu^{2+} on a n-UV LED chip (λ = 395 nm) under a current of 30 mA.

NASO:0.01Eu^{2+} and N-NASO:0.03Eu^{2+} are measured to be 65% and 80%, respectively, which demonstrated the potential application in white LEDs as blue and yellow phosphors pumped by n-UV LEDs chips. Therefore, we combined blue-emitting L-NASO:0.01Eu^{2+}, yellow-emitting N-NASO:0.03Eu^{2+}, and red-emitting Sr[$LiAl_3N_4$]:0.01Eu^{2+} to realize the white light by using the commercial n-UV LED chips (λ = 395 nm). Figure 5b shows the EL spectrum of the packaged WLED device under a forward bias current of 30 mA, and the inset shows the photographs of the fabricated WLED device. The obtained result reveals that the CIE color coordinate is (0.3259, 0.3479) with the white light correlated color temperature (CCT) of 5103 K and a good color rendering index (R_a) of 87. As discussed, $NaAlSiO_4$ phosphors can find promising applications in the fabrication of WLED devices, and two kinds of phosphors originate from one kind of host system that can avoid the inconsistent degradation failure.

CONCLUSIONS

In summary, we have presented a combined theory–experiment approach to investigate the phase selections and structural transformation among the N-, H-, and L-NASO phases from the consideration of the different synthesis temperatures and Eu^{2+}-doping contents in the same $NaAlSiO_4$ system. The crystal structure of L-NASO ($P3_2$) was solved for the first time, and the method on the superstructure peak intensity dependence per temperature, which helps to exclude impurity peaks from the indexing procedure, was suggested and successfully implemented on this example. Moreover, the structure of the parent phase H-NASO was used to solve distorted L-NASO phase. Namely, neglecting these two important facts were the main reason for failing to find symmetry and structure in the past. The similarity between crystal structures of resolved L-NASO and N-NASO phase was finally discovered and topological analysis also supported their close relation, but conformational analysis of topological nets revealed their dissimilarities. The L-NASO phase of Eu^{2+}-doped $NaAlSiO_4$ will transform into N-NASO phase with increasing Eu^{2+} content, ascribed to the mechanical stability in terms of the Debye temperature. Under the excitation of 395 nm, L-

DOI: 10.1021/acs.chemmater.7b02548
Chem. Mater. 2017, 29, 6552–6559

NASO:0.01Eu^{2+} exhibits a blue emission centered at 460 nm with the IQE of 65%, while the N-NASO:0.03Eu^{2+} produces a yellow emission centered at 540 nm with the IQE of 80%, and their photoluminescence behaviors have also been corroborated by DFT calculations on local coordination structures. By integration of the L-NASO:0.01Eu^{2+}, N-NASO:0.03Eu^{2+}, and $Sr[LiAl_3N_4]$:0.01Eu^{2+} phosphors on the *n*-UV LED chips (λ = 395 nm), a white LED device (CIE = (0.3259, 0.3479), R_a = 87, CCT = 5103 K) was obtained. The concept of exploiting phase transition and structural transformation in the solid-state materials will open the gateway for discovering new multicolor phosphors and the tuning of the photoluminescence properties.

■ ASSOCIATED CONTENT

Supporting Information

The Supporting Information is available free of charge on the ACS Publications website at DOI: 10.1021/acs.chemmater.7b02548.

Rietveld refinements, XRD patterns, the corresponding crystal structure diagrams and TG-DTA data of some mentioned samples for Figure S1−S5; main parameters of refinement, coordinates of atoms, and main bond lengths of some mentioned compounds for Tables S1−S6 (PDF)

Crystal structure of $NaAlSiO_4$_(Nepheline) (CIF)

Crystal structure of $NaAlSiO_4$_(low-carnegieite) (CIF)

Crystal structure of $NaAlSiO_4$_(high-carnegeitite) (CIF)

■ AUTHOR INFORMATION

Corresponding Authors

*E-mail: xiazg@ustb.edu.cn (Z. Xia).

*E-mail: ninglx@mail.ahnu.edu.cn (L. Ning).

ORCID

Zhiguo Xia: 0000-0002-9670-3223

Quanlin Liu: 0000-0003-3533-7140

Notes

The authors declare no competing financial interest.

Further details of the crystal structures of N-NASO, L-NASO, and H-NASO may be obtained from Fachinformationszentrum Karlsruhe, 76344 Eggenstein-Leopoldshafen, Germany [fax: (+49)7247-808-666; e-mail: crystdata@fiz-karlsruhe.de; http://www.fiz-karlsruhe.de/request_for_deposited_data.html], quoting the deposition numbers CSD-433180, CSD-433181, and CSD-433182, respectively.

■ ACKNOWLEDGMENTS

The present work was supported by the National Natural Science Foundation of China (Grants 91622125 and 51572023 and 11574003), Natural Science Foundations of Beijing (2172036), and Fundamental Research Funds for the Central Universities (FRF-TP-16-002A3). L.N. acknowledges the support from the Special and Excellent Research Fund of Anhui Normal University.

■ REFERENCES

(1) Kim, Y. H.; Arunkumar, P.; Kim, B. Y.; Unithrattil, S.; Kim, E.; Moon, S. H.; Hyun, J. Y.; Kim, K. H.; Lee, D.; Lee, J. S.; Im, W. B. A zero-thermal-quenching phosphor. *Nat. Mater.* **2017**, *16* (5), 543−550.

(2) Jiang, D.; Jiang, Y. Y.; Li, Z. M.; Liu, T.; Wo, X.; Fang, Y. M.; Tao, N. J.; Wang, W.; Chen, H. Y. Optical Imaging of Phase Transition and Li-Ion Diffusion Kinetics of Single $LiCoO_2$ Nanoparticles During Electrochemical Cycling. *J. Am. Chem. Soc.* **2017**, *139* (1), 186−192.

(3) Kuno, Y.; Tassel, C.; Fujita, K.; Batuk, D.; Abakumov, A. M.; Shitara, K.; Kuwabara, A.; Moriwake, H.; Watabe, D.; Ritter, C.; Brown, C. M.; Yamamoto, T.; Takeiri, F.; Abe, R.; Kobayashi, Y.; Tanaka, K.; Kageyama, H. $ZnTaO_2N$: Stabilized High-Temperature $LiNbO_3$-type Structure. *J. Am. Chem. Soc.* **2016**, *138* (49), 15950−15955.

(4) Chen, M. Y.; Xia, Z. G.; Molokeev, M. S.; Wang, T.; Liu, Q. L. Tuning of Photoluminescence and Local Structures of Substituted Cations in $xSr_2Ca(PO_4)_2$-(1-*x*)$Ca_{10}Li(PO_4)_7$:Eu^{2+} Phosphors. *Chem. Mater.* **2017**, *29* (3), 1430−1438.

(5) Li, D. H.; Wang, G. M.; Cheng, H. C.; Chen, C. Y.; Wu, H.; Liu, Y.; Huang, Y.; Duan, X. F. Size-dependent phase transition in methylammonium lead iodide perovskite microplate crystals. *Nat. Commun.* **2016**, *7*, 11330.

(6) Xia, Z. G.; Liu, G. K.; Wen, J. G.; Mei, Z. G.; Balasubramanian, M.; Molokeev, M. S.; Peng, L. C.; Gu, L.; Miller, D. J.; Liu, Q. L.; Poeppelmeier, K. R. Tuning of Photoluminescence by Cation Nanosegregation in the $(CaMg)_x(NaSc)_{1-x}Si_2O_6$ Solid Solution. *J. Am. Chem. Soc.* **2016**, *138* (4), 1158−61.

(7) Atuchin, V. V.; Gavrilova, T. A.; Gromilov, S. A.; Kostrovsky, V. G.; Pokrovsky, L. D.; Troitskaia, I. B.; Vemuri, R.; Carbajal-Franco, G.; Ramana, C. Low-temperature chemical synthesis and microstructure analysis of GeO_2 crystals with α-quartz structure. *Cryst. Growth Des.* **2009**, *9* (4), 1829−1832.

(8) Xia, Z. G.; Liu, Q. L. Progress in discovery and structural design of color conversion phosphors for LEDs. *Prog. Mater. Sci.* **2016**, *84*, 59−117.

(9) Qin, X.; Liu, X. W.; Huang, W.; Bettinelli, M.; Liu, X. G. Lanthanide-Activated Phosphors Based on 4f-5d Optical Transitions: Theoretical and Experimental Aspects. *Chem. Rev.* **2017**, *117* (5), 4488−4527.

(10) Li, G. G.; Tian, Y.; Zhao, Y.; Lin, J. Recent progress in luminescence tuning of Ce^{3+} and Eu^{2+}-activated phosphors for pc-WLEDs. *Chem. Soc. Rev.* **2015**, *44* (23), 8688−713.

(11) Huang, W. Y.; Yoshimura, F.; Ueda, K.; Shimomura, Y.; Sheu, H. S.; Chan, T. S.; Chiang, C. Y.; Zhou, W. Z.; Liu, R. S. Chemical Pressure Control for Photoluminescence of $MSiAl_2O_3N_2$:Ce^{3+}/Eu^{2+}(M = Sr, Ba) Oxynitride Phosphors. *Chem. Mater.* **2014**, *26* (6), 2075−2085.

(12) Senn, M. S.; Murray, C. A.; Luo, X.; Wang, L. H.; Huang, F. T.; Cheong, S. W.; Bombardi, A.; Ablitt, C.; Mostofi, A. A.; Bristowe, N. C. Symmetry Switching of Negative Thermal Expansion by Chemical Control. *J. Am. Chem. Soc.* **2016**, *138* (17), 5479−82.

(13) Jo, D. S.; Luo, Y.; Senthil, K.; Toda, K.; Kim, B. S.; Masaki, T.; Yoon, D. H. Synthesis and photoluminescence properties of new $NaAlSiO_4$:Eu^{2+} phosphors for near-UV white LED applications. *Opt. Mater.* **2012**, *34* (4), 696−699.

(14) Kim, J.; Kato, H.; Kakihana, M. Control of $NaAlSiO_4$:Eu^{2+} photoluminescence properties by charge-compensated aliovalent element substitutions. *J. Inf. Disp.* **2012**, *13* (3), 97−100.

(15) Pang, R.; Zhao, R.; Jia, Y. L.; Li, C. Y.; Su, Q. Luminescence properties of a new yellow long-lasting phosphorescence phosphor $NaAlSiO_4$:Eu^{2+},Ho^{3+}. *J. Rare Earths* **2014**, *32* (9), 792−796.

(16) Zhao, H. F.; Wang, X. S.; Feng, X. M.; Yao, X. Synthesis and Characterization of a Novel Mechanoluminescence Material $NaAlSiO_4$:Eu^{2+}, Ln^{3+}. *Key Eng. Mater.* **2016**, *680*, 220−223.

(17) Nayak, M.; Kutty, T. Luminescence of Fe^{3+} doped $NaAlSiO_4$ prepared by gel to crystallite conversion. *Mater. Chem. Phys.* **1998**, *57* (2), 138−146.

(18) Han, J. Y.; Im, W. B.; Kim, D.; Cheong, S. H.; Lee, G. Y.; Jeon, D. Y. New full-color-emitting phosphor, Eu^{2+}-doped $Na_{2-x}Al_{2-x}SixO_4$ ($0 \leqslant x \leqslant 1$), obtained using phase transitions for solid-state white lighting. *J. Mater. Chem.* **2012**, *22* (12), 5374.

(19) Cui, D. P.; Xiang, Q. C.; Song, Z.; Xia, Z. G.; Liu, Q. L. The synthesis of narrow-band red-emitting $SrLiAl_3N_4$:Eu^{2+} phosphor and improvement of its luminescence properties. *J. Mater. Chem. C* **2016**, *4* (30), 7332−7338.

(20) Perdew, J. P.; Burke, K.; Ernzerhof, M. Generalized gradient approximation made simple. *Phys. Rev. Lett.* **1996**, *77* (18), 3865.

DOI: 10.1021/acs.chemmater.7b02548
Chem. Mater. 2017, 29, 6552−6559

(21) Canning, A.; Chaudhry, A.; Boutchko, R.; Grønbech-Jensen, N. First-principles study of luminescence in Ce-doped inorganic scintillators. *Phys. Rev. B: Condens. Matter Mater. Phys.* **2011**, *83* (12), 125115.
(22) Dudarev, S.; Botton, G.; Savrasov, S.; Humphreys, C.; Sutton, A. Electron-energy-loss spectra and the structural stability of nickel oxide: An LSDA+ U study. *Phys. Rev. B: Condens. Matter Mater. Phys.* **1998**, *57* (3), 1505.
(23) Blöchl, P. E. Projector augmented-wave method. *Phys. Rev. B: Condens. Matter Mater. Phys.* **1994**, *50* (24), 17953.
(24) Kresse, G.; Furthmüller, J. Efficient iterative schemes for ab initio total-energy calculations using a plane-wave basis set. *Phys. Rev. B: Condens. Matter Mater. Phys.* **1996**, *54* (16), 11169.
(25) Kresse, G.; Joubert, D. From ultrasoft pseudopotentials to the projector augmented-wave method. *Phys. Rev. B: Condens. Matter Mater. Phys.* **1999**, *59* (3), 1758.
(26) Le Page, Y.; Saxe, P. Symmetry-general least-squares extraction of elastic data for strained materials from ab initio calculations of stress. *Phys. Rev. B: Condens. Matter Mater. Phys.* **2002**, *65* (10), 104104.
(27) Hill, R. The elastic behaviour of a crystalline aggregate. *Proc. Phys. Soc., London, Sect. A* **1952**, *65* (5), 349.
(28) Francisco, E.; Blanco, M. A.; Sanjurjo, G. Atomistic simulation of Sr F 2 polymorphs. *Phys. Rev. B: Condens. Matter Mater. Phys.* **2001**, *63* (9), 094107.
(29) Brgoch, J.; DenBaars, S. P.; Seshadri, R. Proxies from ab initio calculations for screening efficient Ce^{3+} phosphor hosts. *J. Phys. Chem. C* **2013**, *117* (35), 17955−17959.
(30) Kumar, A.; Dhoble, S.; Peshwe, D.; Bhatt, J. Structural and Photoluminescence properties of nepheline-structure $NaAlSiO_4:Dy^{3+}$ nanophosphors. *J. Alloys Compd.* **2014**, *609*, 100−106.
(31) Smith, J. V.; Tuttle, O. F. The nepheline-kalsilite system; Part I, X-ray data for the crystalline phases. *Am. J. Sci.* **1957**, *255* (4), 282−305.
(32) Klingenberg, R.; Felsche, J.; Miehe, G. Crystal data for the low-temperature form of carnegieite $NaAlSiO_4$. *J. Appl. Crystallogr.* **1981**, *14* (1), 66−68.
(33) Kovalev, O. V.; Stokes, H. T.; Hatch, D. M. *Representations of the Crystallographic Space Groups: Irreducible Representations, Induced Representations, and Corepresentations*; Gordon and Breach Science: Philadelphia, 1993.
(34) Miller, S. C.; Love, W. F. *Tables of irreducible representations of space groups and co-representations of magnetic space groups*; Pruett Press: Boulder, CO, 1967.
(35) Hatch, D. M.; Stokes, H. T. Practical algorithm for identifying subgroups of space groups. *Phys. Rev. B: Condens. Matter Mater. Phys.* **1985**, *31* (5), 2908.
(36) Allmann, R. Beziehungen zwischen bindungslängen und bindungsstärken in oxidstrukturen. *Monatsh. Chem.* **1975**, *106* (3), 779−793.
(37) Brown, I.; Altermatt, D. Bond-valence parameters obtained from a systematic analysis of the inorganic crystal structure database. *Acta Crystallogr., Sect. B: Struct. Sci.* **1985**, *41* (4), 244−247.
(38) Spek, A. L. PLATON, A Multipurpose Crystallographic Tool, Utrecht University, Utrecht, The Netherlands, 2008; Windows implementation: L. J. Farrugia, University of Glasgow, Scotland, 2008, 40608.
(39) Capillas, C.; Tasci, E. S.; de la Flor, G.; Orobengoa, D.; Perez-Mato, J. M.; Aroyo, M. I. A new computer tool at the Bilbao Crystallographic Server to detect and characterize pseudosymmetry. *Zeitschrift für Kristallographie Crystalline Materials* **2011**, *226* (2), 186−196.
(40) Mackenzie, K. J. D.; Smith, M. E. Multinuclear solid-state NMR of inorganic materials; Pergamon Press: Amsterdam, 2002.
(41) Öhrström, L. Let's Talk about MOFs-Topology and Terminology of Metal-Organic Frameworks and Why We Need Them. *Crystals* **2015**, *5* (1), 154−162.
(42) Li, G.; Lin, C. C.; Chen, W.-T.; Molokeev, M. S.; Atuchin, V. V.; Chiang, C.-Y.; Zhou, W.; Wang, C.-W.; Li, W.-H.; Sheu, H.-S.; et al. Photoluminescence tuning via cation substitution in oxonitridosilicate phosphors: DFT calculations, different site occupations, and luminescence mechanisms. *Chem. Mater.* **2014**, *26* (9), 2991−3001.
(43) Baur, W. H. The geometry of polyhedral distortions. Predictive relationships for the phosphate group. *Acta Crystallogr., Sect. B: Struct. Crystallogr. Cryst. Chem.* **1974**, *30* (5), 1195−1215.
(44) Dorenbos, P. Energy of the first $4f^7 \rightarrow 4f^6 5d$ transition of Eu^{2+} in inorganic compounds. *J. Lumin.* **2003**, *104* (4), 239−260.
(45) Dirksen, G. J.; Blasse, G. Luminescence in the pentaborate $LiBa_2B_5O_{10}$. *J. Solid State Chem.* **1991**, *92* (2), 591−593.
(46) Young, J.; Moon, E. J.; Mukherjee, D.; Stone, G.; Gopalan, V.; Alem, N.; May, S. J.; Rondinelli, J. M. Polar Oxides without Inversion Symmetry through Vacancy and Chemical Order. *J. Am. Chem. Soc.* **2017**, *139* (7), 2833−2841.
(47) Mel'nikova, S.; Molokeev, M.; Laptash, N.; Pogoreltsev, E.; Misyul, S.; Flerov, I. Sequence of phase transitions in $(NH_4)_3 SiF_7$. *Dalton Transactions* **2017**, *46* (8), 2609−2617.
(48) Denault, K. A.; Brgoch, J.; Kloss, S. D.; Gaultois, M. W.; Siewenie, J.; Page, K.; Seshadri, R. Average and local structure, debye temperature, and structural rigidity in some oxide compounds related to phosphor hosts. *ACS Appl. Mater. Interfaces* **2015**, *7* (13), 7264−72.

DOI: 10.1021/acs.chemmater.7b02548
Chem. Mater. 2017, 29, 6552−6559